

Performance and Mix Measurements of Indirect Drive Cu-Doped Be Implosions

D. T. Casey,¹ D. T. Woods,¹ V. A. Smalyuk,¹ O. A. Hurricane,¹ V. Y. Glebov,² C. Stoeckl,² W. Theobald,² R. Wallace,¹ A. Nikroo,³ M. Schoff,³ C. Shulberg,³ K. J. Wu,¹ J. A. Frenje,⁴ O. L. Landen,¹ B. A. Remington,¹ and G. Glendinning¹

¹Lawrence Livermore National Laboratory, Livermore, California 94550, USA

²Laboratory for Laser Energetics, University of Rochester, Rochester, New York 14623, USA

³General Atomics, San Diego, California 92121, USA

⁴Massachusetts Institute of Technology, Cambridge, Massachusetts 02139, USA

(Received 22 October 2014; published 19 May 2015)

The ablator couples energy between the driver and fusion fuel in inertial confinement fusion (ICF). Because of its low opacity, high solid density, and material properties, beryllium has long been considered an ideal ablator for ICF ignition experiments at the National Ignition Facility. We report here the first indirect drive Be implosions driven with shaped laser pulses and diagnosed with fusion yield at the OMEGA laser. The results show good performance with an average DD neutron yield of $\sim 2 \times 10^9$ at a convergence ratio of $R_0/R \sim 10$ and little impact due to the growth of hydrodynamic instabilities and mix. In addition, the effect of adding an inner liner of W between the Be and DD is demonstrated.

DOI: 10.1103/PhysRevLett.114.205002

PACS numbers: 52.57.Fg, 52.70.La

In inertial confinement fusion (ICF) experiments, like those performed at the National Ignition Facility (NIF) [1] and the OMEGA laser facility [2], capsules of deuterium and tritium fuel are imploded to high densities and temperatures to initiate fusion burn. The indirect drive ICF concept uses a laser to irradiate a hohlraum, which produces a nearly uniform thermal x-ray drive. The x-ray drive then ablates the outer capsule material imploding the remaining cryogenically frozen DT shell-mass inward. The conditions necessary for ignition are related to a minimum requirement of the energy density delivered to the DT hot spot and the confinement time of that energy, or equivalently $P\tau$, the product of the hot-spot pressure (P), a measure of the hot-spot energy density, and the energy confinement time (τ) [3]. Betti *et al.* [4] showed that P is related to the implosion velocity (v) by balancing the hot-spot internal energy to the shell kinetic energy via $2\pi PR^3 \sim \theta \frac{1}{2} M v^2$, where R is the radius of the hot spot, θ is the fraction of the shell kinetic energy converted to hot-spot energy, and M is the mass of the shell. Note that assuming a thin shell results in $M \sim 4\pi R^2 \times \rho R$, where ρR is the areal density of the imploded shell. From Newton's law, the hot-spot confinement time is related to the shell inertia like $\tau \sim \sqrt{M/4\pi PR}$. Combining these expressions shows that $P\tau \propto v \times \rho R$ [4]. This means that a successful ignition experiment must achieve high v and high ρR . In the attempt to achieve these conditions, several ablator materials have been considered, i.e., plastic (CH), high density carbon (HDC), and beryllium. The choice of ablator material has important consequences for the implosion hydrodynamics. For example, the mass ablation rate (\dot{m}) can be quite different for different materials. Olson *et al.* [5] measured \dot{m} (in mg/cm²/ns) experimentally and found it to be $0.75T_r^3$ for Be (with and without 1% Cu dopant), $0.50T_r^3$ for HDC, and $0.35T_r^3$ for

CH (0.6% Ge dopant), where T_r is the drive radiation temperature in units of hundreds of eV (or keV). Because the ablation velocity is $V_a = \dot{m}/\rho$, where ρ is the ablator density, Be has the highest V_a for the same in-flight ρ . Also, Lindl *et al.* have shown that the maximum implosion velocity (v_{imp}) depends on the V_a and the in-flight aspect ratio ($R/\Delta R$) like $v_{\text{imp}} \sim 0.56(R/\Delta R)V_a$ [6]. This means that, in principle, Be can achieve higher implosion velocities or operate at lower $R/\Delta R$ for a fixed driver energy. Simakov *et al.* show that the potential benefits of Be target designs still exist even with Cu-doped Be shells currently being considered for ignition experiments [7]. Wilson *et al.* [8] summarized many of the additional mechanical and hydrodynamic advantages of Be, such as high initial density, high tensile strength, and high thermal conductivity. The higher V_a also results in less predicted ablation front instability growth, while designs can also operate at higher remaining mass and lower $R/\Delta R$ for the same implosion velocity. However, Be ablators pose many substantial challenges, particularly in target fabrication [9,10] and Be handling, as well as inhomogeneities that may seed instability growth and mix of ablator material into the hot spot, engineering issues that may negate the more basic plasma physics advantages. Because of these challenges, most NIF experiments to date have been performed with CH [11,12] and HDC [13].

The basic x-ray ablation properties of Be have been studied in mass ablation rate measurements [5], Rayleigh-Taylor growth experiments with planar foils [14–16], and convergent ablator shell-trajectory experiments [17]. However, indirect drive experiments using fusion yield to diagnose implosion performance have not yet been performed. Such experiments are an important step forward, since inhomogeneities in Be crystal structure are of

particularly serious concern and may cause instability growth and mix that will harm overall implosion performance. In addition, the presence of Cu dopant may introduce additional inhomogeneities that could seed instability growth. The results described herein were obtained from indirect drive experiments driven with a two-shock shaped radiation drive and show excellent overall performance. Furthermore, they show the resulting mix of the Cu-doped Be into the hot spot has a negligible impact on the yield at a convergence ratio (initial outer radius/final hot-spot radius) of ~ 10 . These results bolster ongoing efforts [7,18] to develop a Be ignition platform at the NIF. Furthermore, this platform utilized some targets with a thin W tracer layer which provided a valuable test of mix calculations.

The experimental configuration is illustrated in Fig. 1. The laser pulse shape [shown in Fig. 1(a)] is a 2.5 ns long pulse with a ~ 2.5 TW foot and a ~ 20 TW main drive delivered across 40 OMEGA laser beams similar to Ref. [19]. The capsules [details shown in Fig. 1(b)] were 600 μm diameter and 30 μm thick Be shells and were filled with deuterium gas (with trace 0.02 atm of Kr used to measure the capsule leak rate via x-ray fluorescence). The Be capsules were made by coating Be onto a spherical mandrel. The inner 7.5 μm of Be was doped with 4% Cu before removal of the mandrel by pyrolysis to be as relevant as possible to the current Be designs [7,18] and to provide radiographic contrast. After pyrolysis, the Cu dopant diffused into the undoped Be bringing the maximum Cu concentration to 2.5% with a decreasing linear radial gradient toward the outer radius of the capsule. Cross-sectional scanning-electron microscope images of the Be

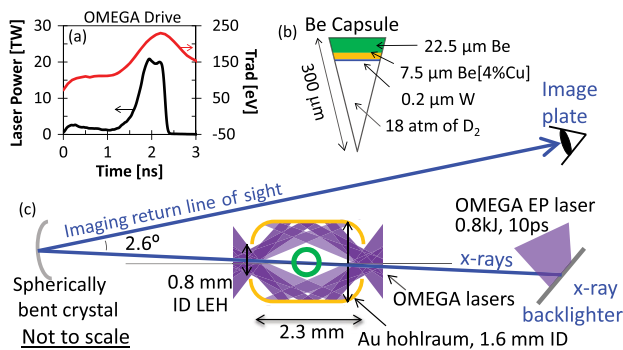


FIG. 1 (color online). Overview of the experimental configuration. (a) Shaped laser pulse shape (black curve) used to produce the hohlraum drive (Omega shape LA232301) and radiation temperature (Tr) obtained by using the DANTE [20,21] diagnostic (red curve). (b) Schematic of the D_2 gas-filled Be capsule. Half of capsules had a 0.2 μm W inner layer. (c) The hohlraum and capsule are backlit by using Cu $k\text{-}\alpha$ x rays produced by using the OMEGA EP laser with a 0.8 kJ, 10 ps, laser pulse. The backlighter x rays are recorded on an image plate by using a spherical crystal imager, which provides a very narrow bandpass image (~ 8 eV).

capsules before and after pyrolysis are shown in Figs 2(a) and 2(b), respectively. Figure 2(c) shows the dopant concentration plotted as a function of radius before and after pyrolysis. Figure 2(c) also shows the amount of trapped Ar gas impurity in the Be resulting from the sputter coating process. Additionally, several targets included thin 0.2 μm thick W layers on the inner capsule surface to provide radiographic contrast and to serve as a gas-shell mix diagnostic (described in detail later). The capsules were driven by 1.6 mm diameter by 2.1 mm long Au hohlraums (50 μm thick) with a 0.8 mm laser entrance hole (LEH).

To observe the capsule in flight, the target was backlit with Cu $k\text{-}\alpha$ x rays produced by the OMEGA extended performance (EP) laser [22,23] delivering a 0.8 kJ, 10 ps, laser pulse onto a 1 mm^2 and 25 μm thick Cu foil. The overall geometry is illustrated in Fig. 1(c). The backlighter x rays are recorded with a spherical crystal imager (SCI) described in detail in Ref. [24], which provides a very narrow bandpass image (~ 8 eV) at 8.05 keV. The SCI uses a quartz crystal with an 88.7° Bragg angle and is 26.7 cm from the target and 393 cm to an image plate detector establishing a magnification of 14.7 [25]. The resolution was determined to be ~ 10 μm using a Au grid with 37 μm hole and a 25 μm bar width.

The SCI view of the capsule through the hohlraum LEH is illustrated in Fig. 3(a) (modeled by VISRAD [26]). The hohlraum axis is tilted 3° from the SCI axis as shown in Fig. 1(c). A 10 ps (duration of the EP backlighter) snapshot image of the imploding capsule, backlit near the peak drive at 2.17 ns with respect to the start of the laser drive, is shown Fig. 3(b). The backlighter x rays are seen through the hohlraum LEHs. The in-flight imploding capsule shell at a convergence ratio of $R_0/R = 1.5$ is clearly seen in the radiograph. Most of the observed contrast is from the thin W layer at the capsule inner surface. A self-emission hot spot is evident in the center of the radiograph from the

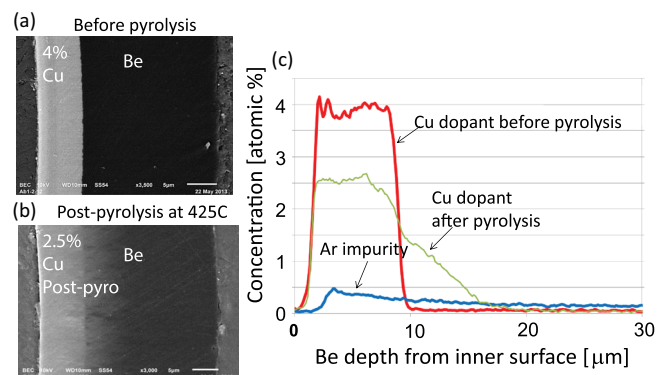


FIG. 2 (color online). (a) A cross-sectional image of the Be capsule before the mandrel is removed by pyrolysis. (b) A cross-sectional image of the Be capsule after the mandrel is removed. (c) Profiles of Cu dopant before and after pyrolysis and of the remnant Ar from the coating process.

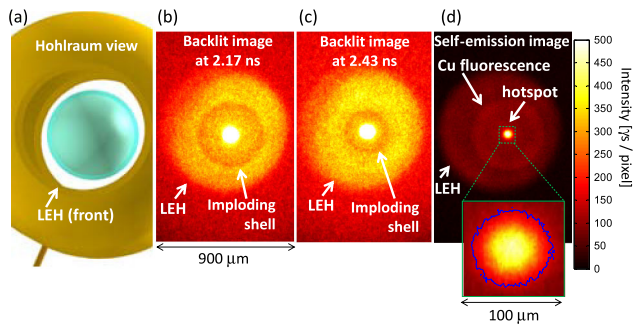


FIG. 3 (color online). (a) View of the capsule with the spherical crystal imager, which is 3° off the hohlraum polar axis. (b) Backlit image of the imploding shell at 2.17 ns using a 10 ps OMEGA EP driven Cu $k\text{-}\alpha$ backlighter. The central feature is the hot-spot self-emission. (c) Backlit image of the imploding shell at 2.43 ns. (d) Time-integrated self-emission image of the capsule. The hot spot is blown up in the lower panel. A 17% intensity contour is illustrated in blue corresponding to a mean hot-spot radius of $38\ \mu\text{m}$. Note that (b)–(d) are on the same color scale but that (d) shows a target without W, which is not as bright as the targets with W, described in more detail in the text. Note also that the color scale for (b) and (c) are saturated to emphasize the imploding shell (making the apparently hot-spot size appear larger by emphasizing lower contours); however, the image plate data are not saturated.

capsule compression. This later-time emission is apparent because, although the backlighter was fired at 2.17 ns for only 10 ps, the image plate is a time-integrated detector. Figure 3(c) shows a radiograph backlit near the end of the drive at 2.43 ns showing the in-flight shell at $R_0/R = 2.1$.

The SCI was also used to image the hot-spot self-emission at peak compression without the EP backlighter. Figure 3(d) shows a self-emission radiograph. The hohlraum outside the LEH casts a distinct shadow. A Cu $K\text{-}\alpha$ fluorescent ring is observed from pumping of the Cu dopant in the Be shell by hot-spot continuum x rays at bang time. An expanded view of the time-integrated hot-spot image is shown in the lower panel. The 17% intensity contour is shown in blue showing a round hot spot with a mean radius of $38\ \mu\text{m}$ from a polar view.

Two-dimensional simulations were performed by using the radiation-hydrodynamics code LASNEX [27]. The calculations included the hohlraum and laser energy deposition using a laser propagation model. All laser power time histories were used as shot; i.e., no adjustment was made to the laser energies to match any of our observations. The impact of turbulence was assessed using a k -epsilon turbulence model [28], where the mix parameters have been validated against Z-pinch experiments.

The measured DD neutron yield, obtained by using the OMEGA nTOF diagnostic suite [29], is shown in Fig. 4(a) as a function of the simulated yield. The red squares are implosions without the $0.2\ \mu\text{m}$ W tracer layer [illustrated in Fig. 1(b)], whereas the blue circles are implosions with the

$0.2\ \mu\text{m}$ W tracer. The shots with W inner layers produced less DD neutron yield, indicating that W mixes into the hot spot and degrades the yield by about a factor of 2. Interestingly, the simulations without including turbulent mix predict a higher yield with the W tracer due to a significantly higher predicted compression. However, including the effects of mix brings the simulated yields much closer to experiment due to enhanced radiative cooling during the high compression phase that effectively quenches the DD burn similar to observations in other experiments [30]. These results show that the W targets are quite sensitive to gas-shell mix and provide a useful test of the mix model. The simulations with mix predict that it has only a small impact for the Be targets without W, when compared to simulations without mix. The hot-spot radii are plotted in Fig. 4(b), determined from self-emission radiographs like shown in Fig. 3(d). Self-emission images were obtained both with and without the W tracer layer on shots without the EP backlighter and used to measure the hot-spot radius defined as the radius of the 17% intensity contour. Implosions with the W tracer layer are larger by $\sim 15\%$, an effect not expected or captured by simulation. This may be due to an apparent increase in radius from multiple localized W bright spots due to breakup of the W layer convolved with the imaging system resolution or that targets with W do not reach as high a compression as those without. Future experiments will be proposed with time-resolved x-ray framing-camera measurements with higher spatial resolution to investigate this issue. The x-ray brightness inferred from the self-emission radiographs showed that targets with W were 6 times brighter at 8 keV than the targets without W. The radial dependence of the x-ray emission is another indicator of turbulent behavior. Simulations without turbulence show evidence of a bright annulus of emission at around 20 microns radius with a slightly depressed core emission, indicative of an intact W liner. By contrast, simulations including turbulence show that at neutron bang time the W remains on the outside of the core but continues subsequently mixing inward, producing a centrally peaked time-integrated x-ray emission, in agreement with the experimental results. The predicted peak x-ray emission occurs after peak neutron emission while the W mix into the core becomes more substantial. Figure 4(c) shows the measured neutron burn weighted bang time, observed using the neutron bang time diagnostics. The targets with the W tracer layer had a somewhat delayed bang time, principally due to the additional payload mass from the very high density W slowing the implosion velocity. Simulations predict that the bang time of these experiments is relatively insensitive to mix. Interestingly, the shot without W with the highest ion temperature [highest solid and open points in Fig. 4(b)] also has the earliest bang time [Fig. 4(c)] and the lowest DD yield [Fig. 4(a)]. The DD burn weighted ion temperature is shown in Fig. 4(d), measured by using the Doppler

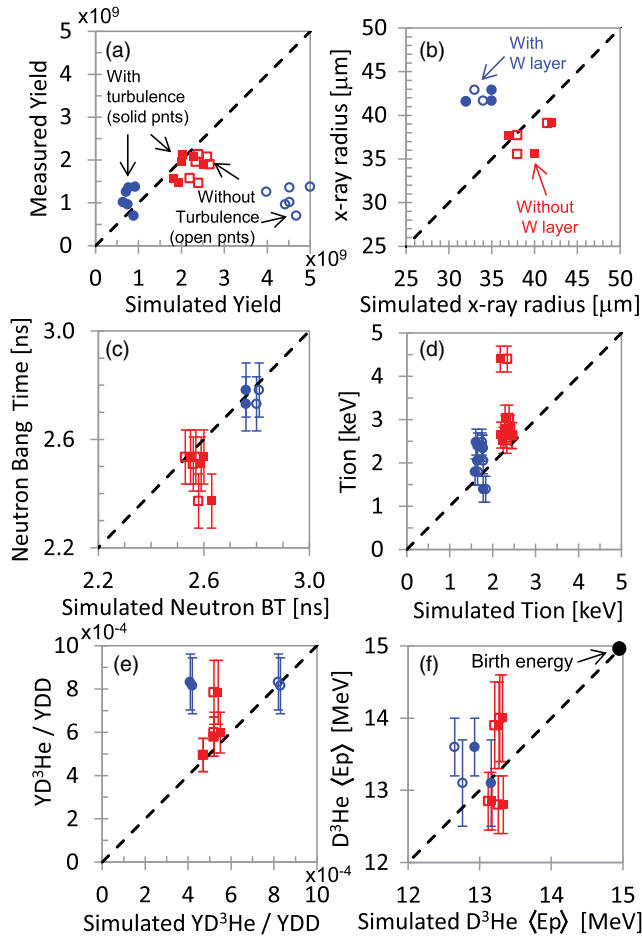


FIG. 4 (color online). Performance observations plotted as a function of simulated observable. In all of the panels, blue points represent targets with a $0.2 \mu\text{m}$ thick W tracer layer on the gas-shell interface, while red squares are without. On the abscissa, solid symbols show simulations that include turbulent mix, while open symbols show simulations without. (a) Measured DD neutron yield from the OMEGA nTOF diagnostic suite [29] as a function of simulated yield. Note the experimental uncertainties are suppressed for clarity and are of the order of the symbol size. (b) Hot-spot radius measured from the x-ray self-emission radiographs with the SCI. Note the experimental uncertainties are suppressed for clarity and are of the order of the symbol size. (c) DD Neutron bang time measured by using the neutron bang time detector. (d) Burn weighted ion temperature measured by using the Doppler broadened 2.45 MeV DD neutron peak observed with the nTOF diagnostics. (e) D^3He proton yield, collected with WRFs over three lines of sight, normalized by the DD neutron yield, which is sensitive to the fuel areal density [31]. (f) Secondary D^3He proton energy measured with three WRFs at different lines of sight, which is sensitive to the total fuel and shell areal densities.

broadened neutron spectrum observed with nTOF detectors. The targets with W tracer layer are $\sim 30\%$ cooler than the targets without due to the slightly heavier shell slowing the implosion velocity. Additionally, simulations predict a weak dependence of ion temperature with and without W

mix, because W mix is predicted to be localized at the gas-shell interface rather than mixed into the central hotter part of the core at the time of neutron production. Secondary D^3He protons were also collected by using wedge range filter (WRF) spectrometers [31], fielded over three lines of sight [using Ten Inch Manipulator (TIM) 1, 2, and 5]. Figure 4(e) shows the measured secondary D^3He proton yield, which is related to deuterium ρR , compared to simulation. The targets without W are in relatively good agreement with simulation, but targets with W are under-predicted, possibly indicating an issue with the transport of ^3He ions in the presence of W mix, the temperature of the unburning mix region, or the calculated hot-spot compression. Figure 4(f) shows the average D^3He proton energy, which is related to the total ρR [31]. The total areal density inferred experimentally from the D^3He proton data averaged over four implosions without the W tracer layer is $66 \pm 10 \text{ mg/cm}^2$, while the total areal density averaged over the implosions with W is $75 \pm 16 \text{ mg/cm}^2$, essentially in agreement within the respective uncertainties indicating that, because of mix, implosions with W reach approximately the same compression as those without (within the uncertainty).

The radial transmission profiles of the radiographs taken with the SCI are shown in Fig. 5(a). The profile shapes are due both to a projection of a 3D spherical shell onto a 2D image plane and the convolution with the instrument resolution. The measured and simulated minimum radius of transmission versus time (including the instrument resolution) is shown in Fig. 5(b). Agreement within $\pm 100 \text{ ps}$ is observed, which is consistent with the bang time comparison. Figure 5(b) also shows simulations including turbulence, which show a minimal effect on the overall shell trajectory.

These Be implosions were comparable to similar CH shell implosions using a similar hohlraum and laser drive [19], which showed DD neutron yields of 1.5×10^9 , ion

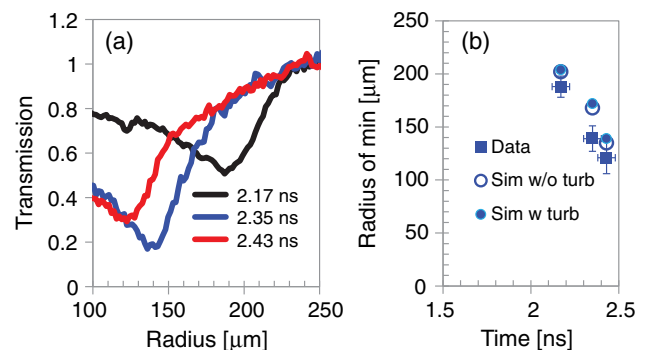


FIG. 5 (color online). (a) Transmission profiles produced from radiographs of the in-flight shell. (b) Measured (square) radius of minimum transmission as a function of time compared with simulations (open circles) and simulations including mix (closed circles).

temperatures of 2.8 keV, and neutron bang times of 2.4 ns. The yield over simulated for the Be targets (without the W tracer layer) is 80%, as compared to CH at $\sim 70\%$ [19].

The data reported here show that indirectly driven Be implosions are well reproduced by simulations at a capsule convergence ratio of ~ 10 . The basic ablation properties of Be [5,8], such as the high ablation velocity, can result in higher velocity and improved stability in simulated ignition designs when compared to CH or HDC designs [7,18]. It is possible that at higher convergence inhomogeneities, sputter material impurities, and dopant nonuniformity may seed unstable growth that could compromise performance. There may also be issues predicting the basic ablation properties of Be and Cu-doped Be such as equation of state, opacity, or thermal conductivity. However, at least at a convergence ratio of ~ 10 these issues do not seem to be significant. This work strongly supports the ongoing efforts to test Be at the more virulent conditions of high convergence at NIF [7,18].

This work also clearly shows that metals layers on the gas-shell interface are unstable (unsurprisingly) and can mix into the hot spot, degrading the performance when compared to clean predictions. There have been suggestions to use the predicted recompression from metal layers to increase overall target performance. However, the effects of mix must be carefully considered first and are likely to significantly degrade the promise of such concepts.

The authors thank the OMEGA and OMEGA-EP scientific and operations staff who supported this work. Helpful conversations with G. Zimmerman, J. Harte, D. Klem, F. Perez, H. Scott, and D. Wilson are also gratefully acknowledged. We also thank M. May for providing the DANTE data analysis. This work was performed under the auspices of the U.S. Department of Energy by Lawrence Livermore National Laboratory under Contract No. DE-AC52-07NA27344.

-
- [1] E. I. Moses, *J. Phys. Conf. Ser.* **112**, 012003 (2008).
 [2] T. R. Boehly *et al.*, *Opt. Commun.* **133**, 495 (1997).
 [3] J. P. Freidberg, *Plasma Physics and Fusion Energy* (Cambridge University Press, Cambridge, England, 2007).

- [4] R. Betti, P. Y. Chang, B. K. Spears, K. S. Anderson, J. Edwards, M. Fatenejad, J. D. Lindl, R. L. McCrory, R. Nora, and D. Shvarts, *Phys. Plasmas* **17**, 058102 (2010).
 [5] R. E. Olson, G. A. Rochau, O. L. Landen, and R. J. Leeper, *Phys. Plasmas* **18**, 032706 (2011).
 [6] J. D. Lindl, P. Amendt, R. L. Berger, S. Gail Glendinning, S. H. Glenzer, S. W. Haan, R. L. Kauffman, O. L. Landen, and L. J. Suter, *Phys. Plasmas* **11**, 339 (2004).
 [7] A. N. Simakov, D. C. Wilson, S. A. Yi, J. L. Kline, D. S. Clark, J. L. Milovich, J. D. Salmonson, and S. H. Batha, *Phys. Plasmas* **21**, 022701 (2014).
 [8] D. C. Wilson *et al.*, *Phys. Plasmas* **5**, 1953 (1998).
 [9] A. Nikroo *et al.*, *Phys. Plasmas* **13**, 056302 (2006).
 [10] A. Nobile *et al.*, *Laser Part. Beams* **24**, 567 (2006).
 [11] M. J. Edwards *et al.*, *Phys. Plasmas* **20**, 070501 (2013).
 [12] O. A. Hurricane *et al.*, *Nature (London)* **506**, 343 (2014).
 [13] A. J. MacKinnon *et al.*, *Phys. Plasmas* **21**, 056318 (2014).
 [14] E. N. Loomis *et al.*, *Phys. Plasmas* **17**, 056308 (2010).
 [15] M. M. Marinak, S. G. Glendinning, R. J. Wallace, B. A. Remington, S. V. Weber, S. W. Haan, and G. W. Collins, *Phys. Plasmas* **9**, 3567 (2002).
 [16] J. A. Cobble *et al.*, *Phys. Plasmas* **13**, 056304 (2006).
 [17] D. G. Hicks *et al.*, *Phys. Plasmas* **17**, 102703 (2010).
 [18] S. A. Yi *et al.*, *Phys. Plasmas* **21**, 092701 (2014).
 [19] J. S. Ross *et al.*, *Sci. Rep.* **3**, 1453 (2013).
 [20] H. N. Kornblum, R. L. Kauffman, and J. A. Smith, *Rev. Sci. Instrum.* **57**, 2179 (1986).
 [21] M. J. May *et al.*, *Rev. Sci. Instrum.* **83**, 10E117 (2012).
 [22] C. Stoeckl *et al.*, *Fusion Sci. Technol.* **49**, 367 (2006).
 [23] L. J. Waxer, D. N. Maywar, J. H. Kelly, T. J. Kessler, B. E. Kruschwitz, S. J. Loucks, R. L. McCrory, D. D. Meyerhofer, S. F. B. Morse, C. Stoeckl, and J. D. Zuegel, *Opt. Photonics News* **16**, 30 (2005).
 [24] C. Stoeckl *et al.*, *Rev. Sci. Instrum.* **83**, 033107 (2012).
 [25] D. B. Sinars, G. R. Bennett, D. F. Wenger, M. E. Cuneo, and J. L. Porter, *Appl. Opt.* **42**, 4059 (2003).
 [26] J. J. MacFarlane, *J. Quant. Spectrosc. Radiat. Transfer* **81**, 287 (2003).
 [27] G. Zimmermann and W. Kruer, *Comments Plasma Phys. Control. Fusion* **2**, 51 (1975).
 [28] J. H. Hammer and G. B. Zimmerman, in *Proceedings of Plasma Physics 47th Annual Meeting, C03.00010* (APS, New York, 2005); LLNL Internal Report No. UCRL-ABS-213676.
 [29] V. Y. Glebov *et al.*, *Rev. Sci. Instrum.* **81**, 10D325 (2010).
 [30] A. R. Miles *et al.*, *Phys. Plasmas* **19**, 072702 (2012).
 [31] F. H. Seguin *et al.*, *Rev. Sci. Instrum.* **74**, 975 (2003).